Chemistry–A European Journal

Research Article
doi.org/10.1002/chem.202303943

Chemistry Europe
European Chemical
Societies Publishing

www.chemeurj.org

Geometric and Electronic Engineering in Co/VN Nanoparticles to Boost Bifunctional Oxygen Electrocatalysis for Aqueous/Flexible Zn-Air Batteries

Zuyang Luo+,[a] Junlin Gong+,[a] Qiuxia Li,[a] Fengli Wei,[a] Baofa Liu,[a] Tayirjan Taylor Isimjan,*[b] and Xiulin Yang*[a]

Modulating metal-metal and metal-support interactions is one of the potent tools for augmenting catalytic performance. Herein, highly active Co/VN nanoparticles are well dispersed on three-dimensional porous carbon nanofoam (Co/VN@NC) with the assistance of dicyandiamide. Studies certify that the consequential disordered carbon substrate reinforces the confinement of electrons, while the coupling of diverse components optimizes charge redistribution among species. Besides, theoretical analyses confirm that the regulated electron configuration can significantly tune the binding strength between the active sites and intermediates, thus optimizing reaction energy barriers. Therefore, Co/VN@NC exhibits a competitive potential difference (ΔE, 0.65 V) between the half-wave potential of ORR and OER potential at 10 mA cm^{-2}, outperforming Pt/C + RuO$_2$ (0.67 V). Further, catalyst-based aqueous/flexible ZABs present superior performances with peak power densities of 156 and 85 mW cm^{-2}, superior to Pt/C-based counterparts (128 and 73 mW cm^{-2}). This research provides a pivotal foundation for the evolution of bifunctional catalysts in the energy sector.

Introduction

The depletion of traditional fuels heralds the future energy revolution dominated by green and renewable technologies.[1] Rechargeable Zn-air batteries (ZABs) are seen as having a bright prospect due to the merits of abundant Zn reserves, excellent theoretical energy density (1086 Wh kg^{-1}), and carbon-free emissions.[2] Nevertheless, severely undesirable activation energy barrier and sluggish kinetics of oxygen reduction and evolution reaction (ORR and OER) during the dis/charge process of air-side electrodes cause ungratified performance.[3] Thus far, although Pt/Ru-group materials are still the optimal and widely ORR/OER catalysts, low-reserve, poor bifunctional activity, and rapid degradation seriously hinder further industrialization.[4] Therefore, designing electrocatalysts with remarkably bifunctional oxygen catalytic activity is crucial to advance energy storage and conversion devices.

At present, transition metal-based materials (Co,[5] Ni,[6] Cu,[7] and Mn[8]) for multiple electrochemical reactions have been inspired by a fast-evolving research field due to the virtues of plentiful reserves and promising activity. Among them, Co features a similar *d*-electron configuration to Pt and thereby has a breathtaking affinity for oxygen-containing intermediates, which is conducive to the elementary reaction in the oxygen-catalyzed process.[9] Regrettably, since a single Co-based catalyst's ORR/OER activity is still insufficient, plentiful strategies have been proposed, such as heteroatomic doping,[10] vacancy regulation,[11] and coupling engineering.[12] Coupling transition metal nitrides (TMNs) and Co-based materials to construct heterojunction can adjust the electronic structure of materials, which is beneficial to optimize the de/adsorption energy of the active centers for reaction intermediate, thus greatly reinforcing the electrocatalytic performance. In TMNs, vanadium nitride (VN) not only possesses high electronic conductivity (~106 s m^{-1}) but also holds better corrosion resistance to improve stability.[13] Moreover, coupling transition metals with N-doped carbon (NC) is also confirmed as a feasible tactic to reinforce the electronic interaction between various components.[14] Meanwhile, due to the diverse morphology and stable properties of NC material, it is beneficial to maximize the exposure of active centers, facilitate mass transfer, and resist chemical corrosion, which is expected to cement the activity and stability of the catalyst.[15]

Here, a bifunctional ORR/OER heterojunction Co/VN@NC nanofoam is synthesized via nitriding metastable cobalt vanadium oxide and dicyandiamide. Experimental and theoretical studies demonstrate the large surface area and interfacial coupling effect in the product, which not only exposes more active sites but also optimizes densities of state/charge. Therefore, Co/VN@NC exhibits a smaller potential difference (ΔE, 0.65 V) between half-wave potential (E$_{1/2}$) and overpotential at 10 mA cm^{-2} (E$_{j10}$) for ORR and OER than commercial Pt/C + RuO$_2$

Chemistry–A European Journal

Research Article
doi.org/10.1002/chem.202303943

Chemistry Europe
European Chemical
Societies Publishing

(0.67 V). Additionally, the Co/VN@NC-based ZAB can achieve a satisfactory open circuit voltage (OCV, 1.41 V) and peak power density (P_{max}, 156 mW cm^{-2}), as well as performing a stability test for 280 h. Meanwhile, a flexible counterpart is assembled, and displays an OCV of 1.34 V and P_{max} of 85 mW cm^{-2}, certifying the promising application in the energy field.

Result and Discussion

In this work, nanofoam-shaped Co/VN@NC is fabricated by a facile two-step method. As illustrated in Figure 1a, a metastable $Co_2V_2O_7$ nanofoam is prepared to refer to our previous work,[16] and can be indexed well with $Co_2V_2O_7$, JCPDS: 70–1189 (Figure S2a). This metastable precursor is then mixed with dicyandiamide for high high-temperature process so that the volatile CN_x can be captured by the oxide to result in the heterogeneous reconstruction of material to Co/VN@NC. This restructured Co/VN@NC can correspond well to Co, JCPDS: 15–0806, VN, JCPDS: 73–0528, C, JCPDS: 75–0444 (Figure 1b). Notably, the height of the C peak in XRD gradually decreases with the increase of temperature, which may originate from the wastage of C (Figure S2b). For comparison, Co@NC and VN@NC are prepared via a similar method. The Raman spectra show that the intensity ratio between D-band (≈ 1337 cm^{-1}, disorder carbon) and G-band (≈ 1586 cm^{-1}, graphitic carbon) for Co/VN@NC is close to 1.36, which is larger than those of Co/VN@NC-750 (1.17), Co/VN@NC-950 (0.92), Co@NC (1.25) and VN@NC (1.10) samples, implying the existence of more defects in Co/VN@NC (Figure 1c and S3).[17] Furthermore, Co/VN@NC displays a larger Brunauer-Emmett-Teller (BET) surface area of 147.5 m^2 g^{-1} than that of the $Co_2V_2O_7$ (1.68 m^2 g^{-1}), which helps to expose more active sites (Figure 1d and S4).[18] Particularly, the mesoporous structure connecting the interior and exterior is further identified by the pore size distribution (≈ 3.8 nm, Figure 1d insert), which can provide abundant channels for the diffusion of reactant molecules, facilitate the de/adsorption of

O_2 to the active center, and transport electrons and mass at the three-phase interface, thus expediting the reaction kinetic.[19]

The morphology of the material is characterized by SEM and TEM. After hydrothermal treatment, the $Co_2V_2O_7$ precursor reveals a three-dimensional (3D) porous nanofoam architecture with spatially staggered interconnecting microchannels (Figures 2a and S5). The TEM images of Co/VN@NC confirms the porous nanofoam is composed of low-magnitude nanoparticles and an outer carbon layer, which is expected to accelerate the mass/electron transfer and ensure the activity of metal in harsh conditions, thus ameliorating the catalyst reaction kinetics and stability (Figures 2b and 2c).[20] Moreover, the HRTEM image and intensity profile of the corresponding areas reveal that lattice spacings of 0.163 and 0.195 nm, are associated with Co and VN (Figure 2d–f). Meanwhile, the SAED pattern confirms that a sequence of diffraction rings can be indexed to the (111) and (200) plane of VN and (220) plane of Co, which is consistent with the results of XRD and HRTEM (Figure 2d insert). Additionally, Figure 2g describes the HAADF-TEM image and its element distribution, proving Co, V, N, and C elements are evenly distributed on the Co/VN@NC porous nanofoam surface.

XPS is employed to delve into chemical states and nuances of electronic interactions. The survey spectra certify the simultaneous presence of Co, V, N, and C elements in the as-prepared materials, aligning with the mapping analysis (Figure S6a). Furthermore, the inductively coupled plasma mass spectroscopy (ICP-MS) is implemented to further identify the actual content of metal elements and indicates the Co and V proportions in Co/VN@NC are 19.3 wt% and 17.8 wt%, respectively (Table S1). As depicted in Figure S6b, the high-resolution C 1s spectrum of as-prepared catalysts are fitted with four functional groups of C=C (284.0 eV), C–C (284.8 eV), C–O/C–N (285.7 eV), and O-C=O (289.0 eV), respectively.[21] The Co 2p spectrum of Co/VN@NC indicates the peak at 777.7 eV is assigned to Co metal. The peaks of Co^{3+} and Co^{2+} appear at 779.8 and 781.5 eV, indicating the possible presence of Co–N bonds (Figure 3a).[22] Furthermore, the binding energy of Co^{3+}
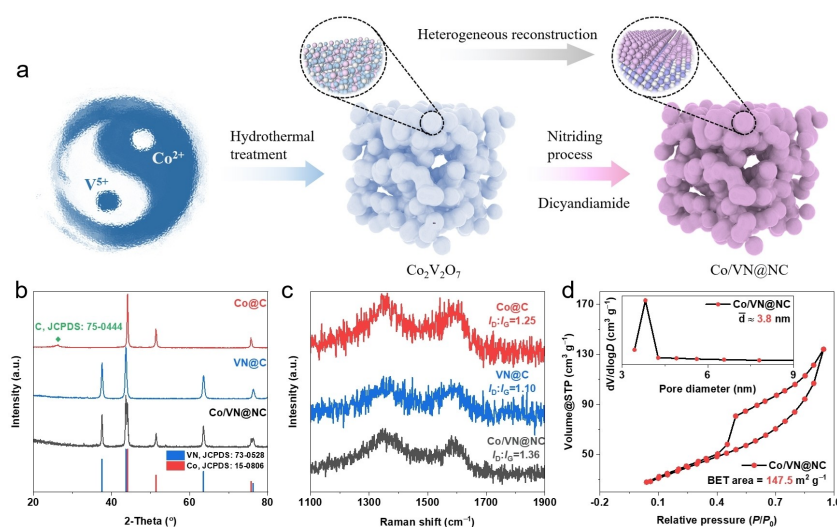

Figure 1. (a) Schematic illustration for synthesizing of Co/VN@NC. (b) XRD patterns and (c) Raman spectra of Co@NC, VN@NC, and Co/VN@NC, respectively. (d) N$_2$ adsorption and desorption isotherms of Co/VN@NC (insert: the corresponding pore size distribution).
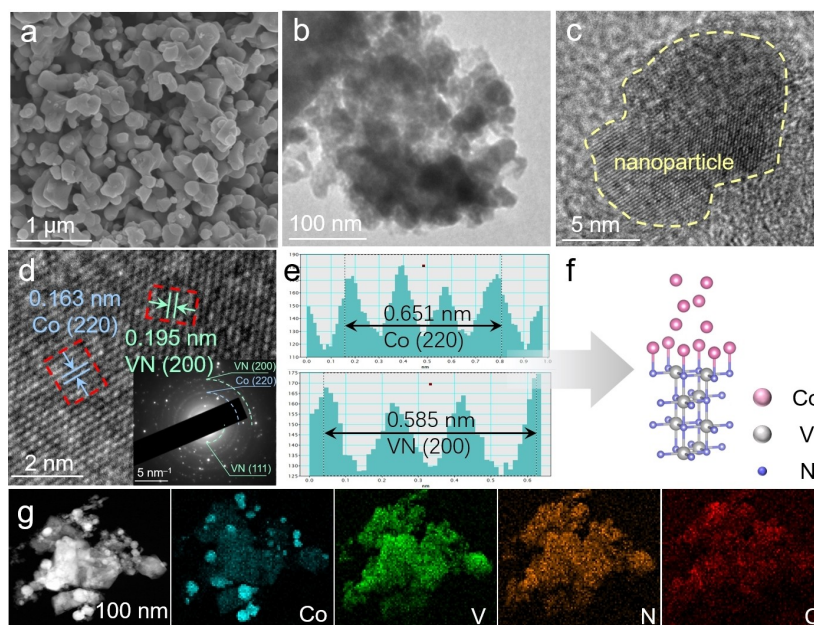
Figure 2. (a) Scanning electron microscopy (SEM), (b) transmission electron microscope (TEM), and (c-d) high-resolution TEM (HRTEM) images of Co/VN@NC (insert: the selected area electron diffraction (SAED) pattern). (e) Intensity profile of corresponding areas in Figure 2d. (f) DFT calculated model. (g) High-angle annular dark-field scanning TEM (HAADF-TEM) and corresponding elemental distribution images.
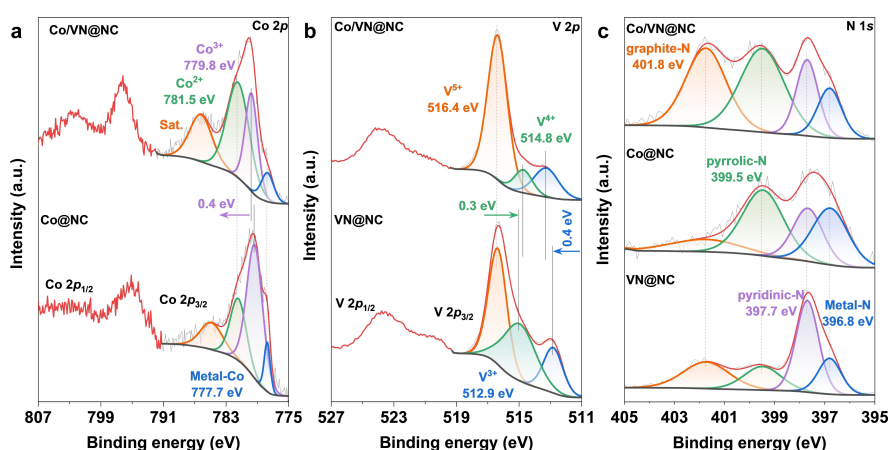

Figure 3. High-resolution X-ray photoelectron spectroscopy (XPS) spectra of (a) Co 2p, (b) V 2p, and (c) N 1s regions in Co/VN@NC, Co@NC, and VN@NC, respectively.

in Co/VN@NC is elevated by 0.4 eV compared to Co@NC. Meanwhile, in the V 2p regions of both Co/VN@NC and VN@NC (Figure 3b), the peaks at 516.4, 514.8, and 513.3 eV are indexed to the V^{5+}, V^{4+}, and V^{3+}, respectively.[23] Interestingly, the binding energies of V^{4+} and V^{3+} shift negatively by 0.3 eV and positively by 0.4 eV, respectively, compared with VN@C. This fluctuation in binding energy for Co and V spectra showcases a prominent electronic interaction within the heterostructure.[22] Notably, the interaction stemming from charge redistribution, not only accelerates charge transfer but also fine-tunes the electron configuration, ultimately enhancing oxygen catalytic kinetics.[24] For N 1s spectra (Figure 3c), peaks at binding energies of 396.8, 397.7, 399.5, and 401.8 eV are representative of metal-N, pyridinic-N, pyrrolic-N, and graphitic-N, respectively.[25] Generally, the pyridinic-N and pyrrolic-N can

create ample defects within the carbon matrix to act as the active species of ORR. The graphitic-N can increase the charge density of the π-conjugated system, thus hastening electron transportation and reinforcing conductivity.[26] As expected, XPS analysis further underscores the successful synthesis of heterostructure and incorporation of VN, resulting in an optimized charge density, thereby augmenting the catalyst's inherent activity.

ORR measurements are executed in 0.1 M KOH solution (N_2/O_2-saturated). The optimal catalyst (noted as Co/VN@NC) is obtained at the calcination temperature of 850 °C (Figure S7). As evidenced in Figure 4a, CV curves of catalysts exhibit distinct reduction peaks in the O_2-saturated electrolyte compared to the N_2-saturated counterpart, confirming the selectivity of catalysts for oxygen reduction.[27] Interestingly, an appreciable oxidation
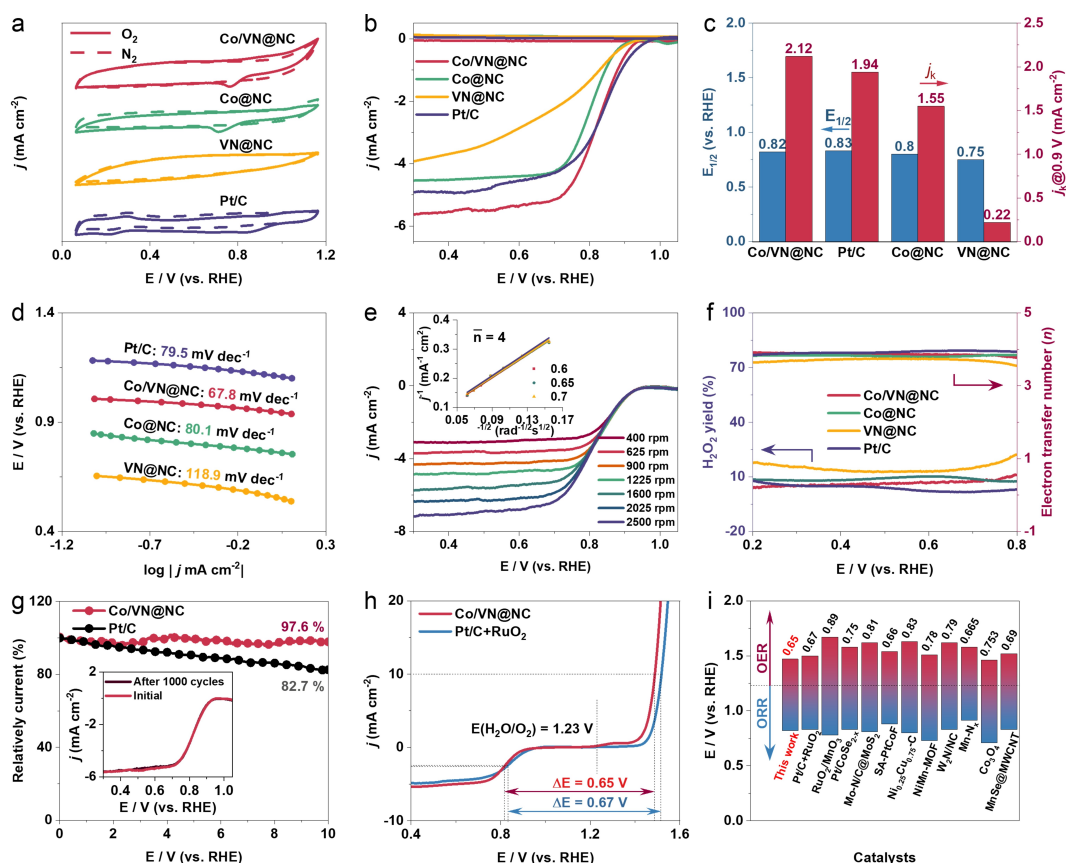
Chemistry–A European Journal | Research Article
doi.org/10.1002/chem.202303943

Chemistry
Europe
European Chemical
Societies Publishing

Figure 4. (a) ORR CV curves, (b) LSV curves, (c) summary of the corresponding $E_{1/2}$ and j_k values, and (d) Tafel plots. (e) Polarization curves of Co/VN@NC at various rotating speeds (insert: the corresponding K–L plots). (f) H_2O_2 yield (%) and electron transfer number (n). (g) CP response (insert: LSV curves of before and after 1000 cycles). (h) Overall polarization curves of Co/VN@NC and Pt/C + RuO_2 for bifunctional catalytic activity tests. (i) Comparison of ΔE ($\Delta E = E_{j10} - E_{1/2}$) between Co/VN@NC and other catalysts.

peak is observed in Co@NC, but not for VN@NC, which implies Co species are likely to play a predominant role to drive the ORR process. According to the linear sweep voltammetry (LSV) polarization curves obtained at 1600 rpm, Co/VN@NC manifests a more positive onset potential (E_{onset}) of 0.94 V and $E_{1/2}$ of 0.82 V, compared to those of Co@NC (0.92 V, 0.80 V), VN@NC (0.92 V, 0.75 V), $Co_2V_2O_7$ (0.65 V, 0.57 V) and most recently reported electrocatalysts (Table S2), whereas slightly lower than Pt/C (0.97 V, 0.83 V) (Figure 4b and S8). Additionally, Co/VN@NC has the largest limiting current density ($j_L = 5.67$ mA cm^{-2}) among these samples. Typically, the theoretical limiting current density is certified as 5.97 mA cm^{-2}.[28] This discrepancy may be due to the difference between the practical and theoretical environment.[29] Distinctly, two reduction peaks appear at about 1.03 V in the LSV curves of Co/VN@NC and Co @NC, which is basically consistent with the potential range of the transformation of Co^{2+} and Co^{3+} (Figure S9).[30] Moreover, the kinetic current density (j_k) of composite material soars to 2.12 mA cm^{-2} at 0.9 V overshadowing both Co@NC (1.55 mA cm^{-2}) and VN@NC (0.22 mA cm^{-2}), explicating that the superior kinetics of Co/VN@NC (Figure 4c). In parallel, the Tafel slope value of Co/VN@NC (67.8 mV dec^{-1}) is lower than that of Co@C (80.1 mV dec^{-1}), VN@NC (111.9 mV dec^{-1}) and the benchmark Pt/C (79.5 mV dec^{-1}), suggesting more favorable ORR kinetics

(Figure 4d).[31] The above results illustrate that Co/VN@NC bears a favorable activity, which is attributed to the strong electronic interaction induced by the introduction of VN and the porous sponge architecture that is essential for exposing more active sites.[32]

The reaction mechanism underlying Co/VN@NC is elucidated by the RDE technique. As illustrated in Figure 4e, the Koutecky–Levich (K–L) plot with good linearity is obtained by recording LSV curves across diverse rotation speeds, which abides by the first-order reaction kinetics of ORR. The electron transfer number (n) is approximately 4 according to the result of the K–L equation, signifying that the ORR process follows a four-electron transfer pathway. The RRDE technique is employed to further decipher the reaction mechanism (Figure 4f). The value of n is evaluated to be 4, being consistent with the RDE analysis. Simultaneously, the H_2O_2 yield of Co/VN@NC ($<$ 10 %) is visibly lower than that of Co@NC and VN@NC, exemplifying that the coupling effect between Co and VN has an indispensable influence on the selectivity of the product.[33] To further probe the origin of electrochemistry activity, the ECSA is gauged by the value of the electric double-layer capacitance (C_{dl}). C_{dl} is obtained ground on CV curves at various scan rates from 5 to 30 mV s^{-1} (Figure S8). The Co/VN@NC arises a C_{dl} value of 19.5 mF cm^{-2}, outperforming those of Co@NC

Chem. Eur. J. **2024**, e202303943 (4 of 9)

© 2024 Wiley-VCH GmbH

(0.7 mF cm^{-2}) and VN@NC (0.6 mF cm^{-2}), meaning that more active sites can be exposed to contact with reactants (Figure S10 and S11).[26] Such results underscore the expansive specific surface area of Co/VN@NC, enhanced by its unique 3D porous nanofoam.

Stability undeniably stands as a critical criterion when assessing catalysts. As presented in Figure 4g, the robust stability of Co/VN@NC is testified by a current retention of 97.6% after the chronoamperometric response of 10 h compared to that of Pt/C (82.7%). Meanwhile, the LSV curve of Co/VN@NC fails to change significantly after 1000 cycles of CV testing, further confirming its superior stability (Figure 4g insert). Post ORR chronoamperometric (CP) stability testing, the morphology, crystal structure, and chemical valence state of Co/VN@NC were characterized. SEM imaging verifies the preservation of the nanofoam structure post-stability testing. (Figure S12). Moreover, XRD analysis affirms that, even after a 10 h operational period, the crystal structure closely aligns with the pre-stability test sample (Figure S13). Only minimal alterations are observed in the chemical composition of the catalyst's surface. After the stability test, XPS spectrum analysis identifies the presence of Co 2p, V 2p, C 1s, and N 1s. Interestingly, there's a slight increase in the proportions of the lower valence state metals, metal-N, and pyridinic-N, resulting from the ORR-reducing environment (Figure S14).[34] The distinguished durability of the Co/VN@NC catalysts can be ascribed to the unique hierarchical morphology of the porous nanofoam in the catalysts and the protection of the NC layer, which can prevent metal migration and aggregation during electrocatalytic process via stabilizing accessible active sites.[35]

The overall bifunctional electrocatalytic performance is also evaluated by the ΔE between $E_{1/2}$ and E_{j10}. As shown in Figure 4h, Co/VN@NC boasts the lowest ΔE of only 0.65 V, which is much smaller than that of commercial Pt/C + RuO$_2$ (0.67 V). Moreover, this ΔE of 0.65 V also outperforms nearly all of the state-of-the-art bifunctional oxygen catalysts (Figure 4i, Table S3), suggesting the superior advantages of Co/VN@NC in rechargeable ZABs.

To give a quantified illustration of the chemical property and activity mechanism of catalysts, theoretical investigations are employed based on the chemical environment information of Co/VN@NC. The electron localization function analysis and the differential charge density isosurfaces induced by the introduction of VN into the Co sites have been calculated, which finds a reinforced charge interaction occurs between Co and V, expected to facilitate the adsorption of O$_2$ (Figure 5a). Furthermore, the density of states (DOS) is implemented to appraise the binding strength of the metal center for oxygen-containing intermediates and electronic transfer capacity.[36] As illustrated in Figure 5b, a more positive d-band center (0.07 eV) is displayed by the Co site, compared with the V site (-0.01 eV), implying a more suitable affinity for O$_2$.[37] Meanwhile, a broader region near the Fermi level for composite material implies a reinforced metallicity, which is expected for faster electron transfer.[38]
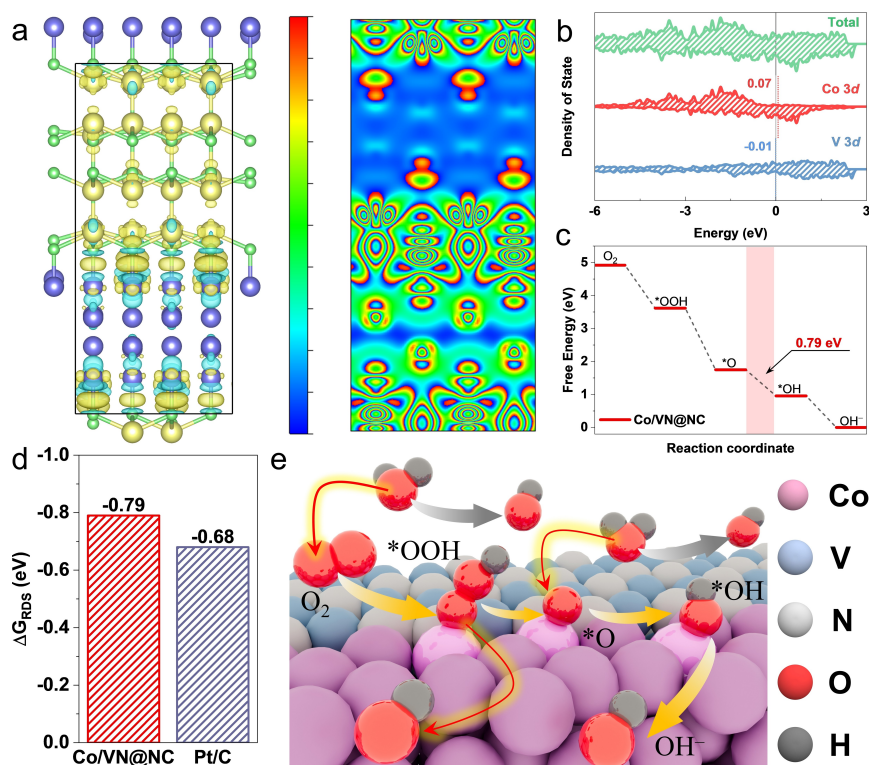

Figure 5. (a) Calculated charge density differences and corresponding sliced electron localization function for CoP/V(PO$_3$)$_3$@HCS (Cyan region represents the depletion of electrons, and the yellow represents the accumulation of electrons). (b) DOS profit, (c) free energy diagrams, (d) summarized ΔG_{RDS} values, and (f) schematic diagram of reaction pathways.

Chemistry–A European Journal

Research Article
doi.org/10.1002/chem.202303943

Chemistry Europe
European Chemical
Societies Publishing

The reaction mechanism of forming H_2O from O_2 in alkaline media is depicted in Figure 5e. The corresponding changes in free energy at U = 0 and 1.23 V are calculated in Figures 5c and S13. Typically, the proposed ORR mechanism includes four steps: hydrogenation of O_2 into *OOH, break of O—O bond to transform *OOH into *O, protonation of *O to *OH, and the desorption of surface-bound *OH to create OH^-.[39] A desired ORR electrocatalyst is characterized by minimal Gibbs free energy differences in the rate-determining step (ΔG_{RDS}), approaching −1.23 (U = 0 V) and 0 eV (U = 1.23 V), respectively. This criterion ensures that the electrocatalyst is capable of efficiently promoting the ORR process. For Co/VN@NC, the RDS is the third step of electron transport progress (*O + H_2O + e^- → *OH + OH^-) with corresponding ΔG_{RDS} values of −0.79 eV (U = 0 V) and 0.54 eV (U = 1.23 V). Notably, these ΔG_{RDS} values are lower than those reported of Pt in the literature (−0.68 eV and 0.61 eV) (Figure 5d and S13).[40] The above discussion suggests a shrunk ΔG_{RDS} value of Co/VN@NC, which implies faster reaction kinetics, in line with the electrochemistry section.

According to the above discussion, the extraordinary ORR/OER activity and stability of Co/VN@NC are considered as being caused by the following factors: (1) The 3D rich-porous architecture with a high specific surface area can accelerate the transport of mass and amplify the utilization rate of Co. (2) The engineered electronic structure of the metal sites can steer the charge redistribution to optimize the adsorption/desorption of oxygen intermediates. (3) The NC layer has strong corrosion resistance and can stabilize the active center well in harsh electrochemical environments.

To investigate the industrial viability of the resultant bifunctional catalysts, a rechargeable ZAB is fabricated (Figure 6a). As depicted in Figure 6b, Co/VN@NC-based ZAB is capable of delivering a higher OCV of 1.41 V than Pt/C (1.35 V). Expectedly, the battery equipped with Co/VN@NC displays a P_{max} of 156 mW cm^{-2} (Figure 6c), greatly outclassing Pt/C + RuO$_2$ (128 mW cm^{-2}) and many previously reported catalysts (Table S4). The specific capacitance curves are presented grounding on a normalized mass of consumed Zn (Figure 6d). The specific capacity of Co/VN@NC-based ZAB is
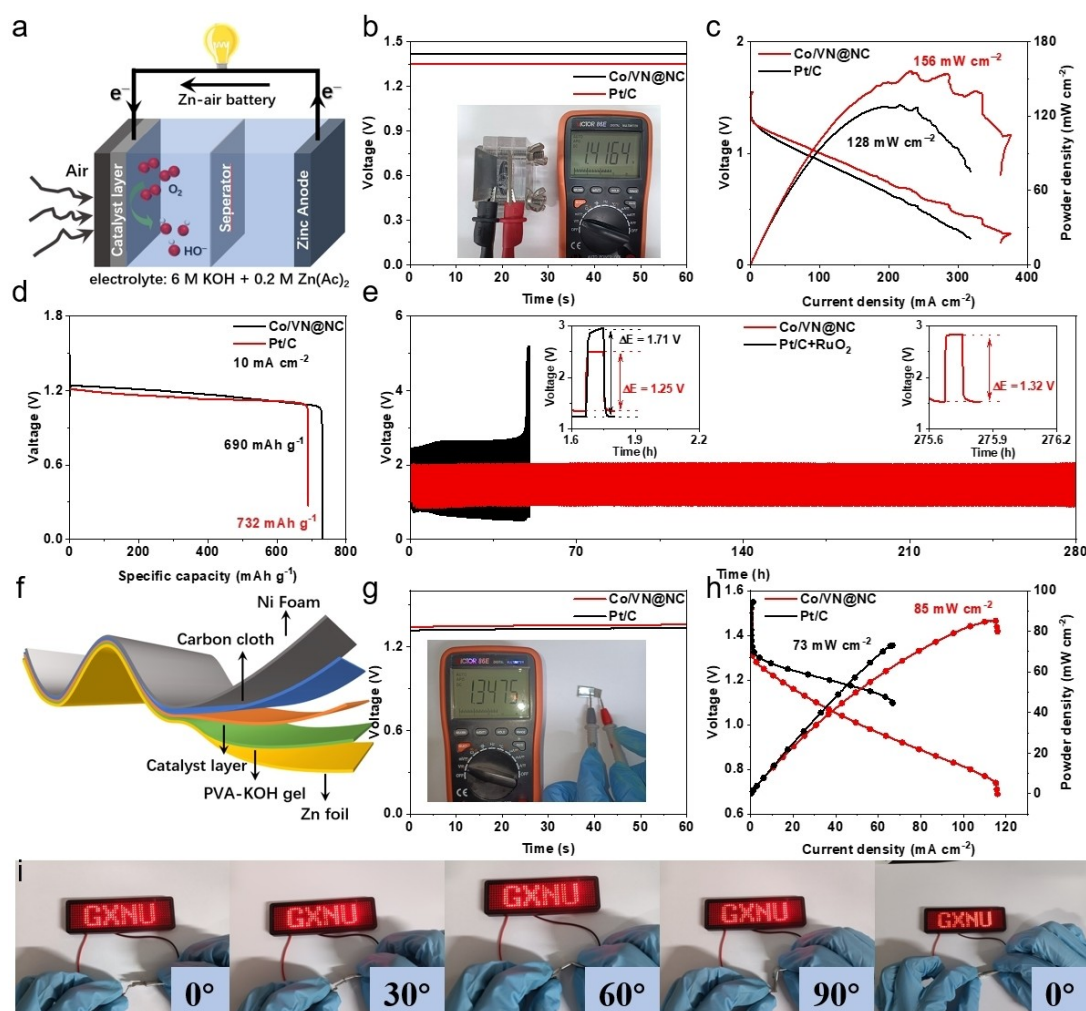

Figure 6. (a) Schematic illustration of aqueous ZAB. (b) OCV plots. (c) Discharge polarization curves and powder density plots. (d) Specific capacity plots. (e) Galvanostatic charge-discharge cycling at 5 mA cm^{-2} (insert: the curves at start and end of tests). (f) Configuration, (g) OCV plots, (h) discharge polarization curves, and powder density curves of flexible ZAB. (i) Photos of LED panels powered by flexible ZAB at different folding angles of 0°, 30°, 60°, 90° and back to 0°.

Chem. Eur. J. **2024**, e202303943 (6 of 9)

© 2024 Wiley-VCH GmbH

Chemistry–A European Journal

Research Article
doi.org/10.1002/chem.202303943

Chemistry Europe
European Chemical
Societies Publishing

866.1 mAh g^{-1} (theoretical energy density: $1601.9 \text{ mWh g}^{-1}$), which is better than $Pt/C + RuO_2$ catalysts (690.3 mAh g^{-1}, $1276.8 \text{ mWh g}^{-1}$). The assembled ZAB features a minimal voltage gap of 1.25 V corresponding to $E_{discharge}/E_{charge}$ (Figure 6e), markedly superior to the Pt/C (1.71 V). After operating, the charge and discharge cycle for 280 h, the voltage gap only widens by 0.07 V (5.6%), reflecting its promising industrial potential. The wearability of ZAB is another essential factor that should be verified for practical application (Figure 6f). As shown in Figure 6g, the OCV of the as-equipped flexible ZAB by Co/VN@NC is 1.34 V, marginally surpassing the Pt/C (1.32 V). Remarkably, Figure 6h highlights a more conspicuous P_{max} of 85 mW cm^{-2} for Co/VN@NC, which is much better than that of Pt/C (73 mW cm^{-2}). Furthermore, this flexible ZAB can smoothly light the LED panel at different bending angles (0°, 30°, 60°, 90°), further verifying its mechanical flexibility. Remarkably, the LED remains illuminated even when returned to a 0° angle (Figure 6i). To sum up, the well-designed heterogeneous Co/VN@NC electrode demonstrates immense promise for application in affordable energy storage solutions and portable electronics.

Experimental Section

Materials

Cobalt chloride hexahydrate ($CoCl_2 \cdot 6H_2O$, 99.0%), ammonium metavanadate (NH_4VO_3, 99.0%), and dicyandiamide are analytical reagents and used without further purification.

Synthesis of $Co_2V_2O_7$ precursor

0.8 mmol $CoCl_2$ and 0.8 mmol NH_4VO_3 are dissolved into 60 mL deionized (DI) water with agitating at 70 °C for 10 min. Afterward, the above solution was transferred into a 100 mL autoclave to heat at 180 °C for 18 h. After cooling, the resulting $Co_2V_2O_7$ powder is collected by centrifuging, washed with DI water 3 times, and dried at 60 °C overnight.

Synthesis of Co/VN@C catalysts

60 mg $Co_2V_2O_7$ powder and 100 mg dicyandiamide are ground thoroughly for 10 min. Next, the obtained mixed powder is heated at the temperature of 750, 850, and 950 °C for 2 h under Ar ($5°C \text{ min}^{-1}$) to obtain Co/VN@C-750, Co/VN@C, and Co/VN@C-950. For comparison, Co@C or VN@C is synthesized by grinding $CoCl_2$ or VCl_3 with dicyandiamide, followed by pyrolysis.

Assembly and test of aqueous ZAB

The performance test of ZAB is carried out on the LAND-BT2016 A workstation. The catalyst is configured as ink, and cast on carbon paper as an air cathode, and a polished Zn plate as an anode. Additionally, $6 \text{ M KOH} + 0.2 \text{ M Zn(CH}_3\text{COO)}_2$ is used as an electrolyte. For comparison, 20 wt% Pt/C is involved.

Assembly and test of flexible ZAB

5 g Polyvinyl alcohol is dissolved in 50 mL DI water at 90 °C with stirring for 1.5 h to obtain a gel polymer electrolyte. Afterward, a mixed solution of 18 M KOH and 0.02 M $Zn(CH_3COO)_2$ is poured into the above gel, stirred for 30 min, and frozen at −20 °C to form the final electrolyte gel. Ultimately, this prepared gel, a piece of carbon-supported catalyst as an air cathode, and a polished Zn foil are assembled into a flexible ZAB.

Electrochemical measurements

ORR tests are conducted on a CHI 760E electrochemical workstation with a three-electrode system. Ag/AgCl electrode and graphite rod are regarded as the reference electrode and auxiliary electrode, respectively. The rotating ring disk electrode (RRDE, diameter = 5.61 mm, PINE instruments) and rotating disk electrode (RDE, diameter = 5 mm, PINE instruments) loaded with catalyst ink are used as the working electrode. To form a well-distributed catalyst ink, 2 mg electrocatalyst is dispersed into a mixed solution (containing 200 μL isopropanol, 200 μL DI water, and 5 μL 5 wt% Nafion) and ultrasonication for 1 h. Afterward, 25 μL catalyst ink is pipetted onto the surface of RDE and RRDE, respectively. The measured potential is converted to the reversible hydrogen electrode (RHE) from the Nernst equation (Figure S1a):

$$E_{RHE} = E_{Ag/AgCl} + 0.059pH + 0.196$$

Cyclic voltammetry (CV) measurements are carried out in O_2 or N_2-saturated 0.1 M KOH solution with a scan rate of 50 mV s^{-1}. Linear sweep voltammetry (LSV) curves are obtained at a sweep rate of 10 mV s^{-1} with various rotation speeds (400–2025 rpm) and the potential range from −0.9 to 0.2 V. The long-term stability measurements are performed by using chronoamperometry in O_2-saturated 0.1 M KOH at a rotation speed of 1600 rpm. The Tafel slopes are given by the equation:

$$\eta = b \log\left(\frac{j}{j_0}\right)$$

The number of electrons transferred (n) is determined in combination with the RDE test by the Koutechy-Levich (K–L) equation:

$$\frac{1}{j} = \frac{1}{j_k} + \frac{1}{B\omega^{1/2}}$$

$$B = 0.62nFC_0\nu^{-1/6}D_0^{2/3}$$

Where j and j_k represent the measured and kinetic current density (mA cm^{-2}), respectively. ω is the angular velocity, n is the electron transfer number of O_2, F is the Faraday constant (F = 96485 C mol^{-1}), C_0 and D_0 are the bulk concentration (1.2×10^{-3} mol L^{-1}) and diffusion coefficient (1.9×10^{-5} cm^2 s^{-1}) of O_2 in 0.1 M KOH, ν is the dynamic viscosity (0.01 cm^2 s^{-1}).

The percentage of H_2O_2 yield (%) and n during ORR were calculated in combination with RRDE test results according to the following equations:

$$n = 4\frac{I_d}{I_d + I_r/N}$$

$$H_2O_2(\%) = 200 \frac{I_r/N}{I_d + I_r/N}$$

Where I_d and I_r denote the disk and ring currents, respectively.

The OER polarization curve is tested and calibrated by a Biologic VMP3 electrochemical workstation in a 1.0 M KOH electrolyte (Figure S1b).

Conclusions

In summary, the Co/VN@NC OER/ORR bifunctional electrocatalyst has been synthesized via two viable hydrothermal and nitriding steps. During this course, cobalt vanadium oxides mighty trap CN_x species released from the decomposition of dicyandiamide under high-temperature conditions and in situ reconstitute into heterostructures. Additionally, the CO_2 generated plays a pivotal role in creating the porous architecture. Spectroscopic evaluations underscore pronounced electron interactions between metal species due to a coupling effect, thus optimizing the adsorption of reaction intermediates. Meanwhile, the theoretical investigation further suggests that composite achieves an optimized density of state and a reduced activation energy barrier. Therefore, Co/VN@NC exhibits a superior ORR and OER activity with a shrunk difference between the half-wave potential and overpotential at 10 mA cm^{-2}. Moreover, Co/VN@NC-based aqueous/flexible ZAB can deliver an impressive power density. These findings chart a promising path for the design and development of potent catalysts in the energy domain.

Conflict of Interests

The authors declare no conflict of interest.

Data Availability Statement

The data that support the findings of this study are available from the corresponding author upon reasonable request.

[1] a) X. Wang, X. Zhou, C. Li, H. Yao, C. Zhang, J. Zhou, R. Xu, L. Chu, H. Wang, M. Gu, H. Jiang, M. Huang, *Adv. Mater.* **2022**, *34*, 2204021; b) H. Han, Y. Wang, Y. Zhang, Y. Cong, J. Qin, R. Gao, C. Chai, Y. Song, *Acta Phys.-Chim. Sin.* **2020**, *0*, 2008017; c) L. Li, S. Shen, G. Wei, J. Zhang, *Acta Phys.-Chim. Sin.* **2021**, *37*, 1911011; d) N. Tanjedrew, K. Thammanatpong, P. Surawatanawong, P. Chakthranont, T. Chantarojsiri, T. Unjarern, S. Kiatisevi, *Chem. Eur. J.* **2024**, *30*, e202302854.

[2] a) M. Guo, Z. Huang, Y. Qu, L. Wang, H. Li, T. T. Isimjan, X. Yang, *Appl. Catal. B* **2023**, *320*, 121991; b) S. Huang, W. Zhang, G. Zhuang, P. Wang, Q. Chen, S. Zhou, X. Han, *Chem. Eur. J.* **2023**, *29*, 202300321; c) W. Zhang, S. Xie, S. Wang, P. Zhao, X. Yang, P. Huang, P. Liu, F. Cheng, *Chem. Eur. J.* **2023**, *29*, 202203787; d) H. Xue, J. He, K. Chang, P. Li, T. Wang, T. Zhang, X. Fan, X. Li, Y. Xu, *Nano Research Energy* **2023**, *2*, e9120052.

[3] T. Liu, Y. Wang, Y. Li, *Adv. Funct. Mater.* **2022**, *32*, 2207110.

[4] a) H. Singh, M. Marley-Hines, S. Chakravarty, M. Nath, *J. Mater. Chem. A* **2022**, *10*, 6772; b) L. Qi, T. T. Isimjan, Z. Huang, M. Liao, L. Wang, X. Yang, *Chem. Eur. J.* **2023**, *29*, 202301521.

[5] Y. Yang, R. Zeng, Y. Xiong, F. J. DiSalvo, H. D. Abruna, *J. Am. Chem. Soc.* **2019**, *141*, 19241.

[6] W. Wang, J. Cai, H. Wan, W. Cai, Z. Zhu, C. Wang, T. Zhou, Z. Hou, Y. Zhu, Y. Qian, *J. Mater. Chem. A* **2022**, *10*, 14613.

[7] R. Chen, T. Shu, F. Zhao, Y. Li, X. Yang, J. Li, D. Zhang, L.-Y. Gan, K. X. Yao, Q. Yuan, *Nano Res.* **2022**, *15*, 9010.

[8] Y. Pei, D. P. Wilkinson, E. Gyenge, *Small* **2023**, *19*, 2204585.

[9] C. Zhang, L. Yuan, C. Liu, Z. Li, Y. Zou, X. Zhang, Y. Zhang, Z. Zhang, G. Wei, C. Yu, *J. Am. Chem. Soc.* **2023**, *145*, 7791.

[10] E. Y. Choi, D. E. Kim, S. Y. Lee, C. B. Park, C. K. Kim, *Appl. Catal. B* **2023**, *325*, 122386.

[11] H. Tian, A. Song, P. Zhang, K. Sun, J. Wang, B. Sun, Q. Fan, G. Shao, C. Chen, H. Liu, Y. Li, G. Wang, *Adv. Mater.* **2023**, *35*, 2210714.

[12] F. Gui, Q. Jin, D. Xiao, Z. Jin, Y. Zhang, Y. Cao, M. Yang, Q. Tan, C. Zhang, S. Siahrostami, Q. Xiao, *J. Mater. Chem. A* **2023**, *11*, 1312.

[13] a) J. Feng, R. Tang, G. Liu, T. Meng, *Chem. Eng. J.* **2023**, *452*, 139131; b) J. Zhao, Y. Zhao, W. Yue, X. Li, N. Gao, Y. Zhang, C. Hu, *Chem. Eng. J.* **2022**, *441*, 136082.

[14] D. Li, J. Liang, S. J. Robertson, Y. Chen, N. Wang, M. Shao, Z. Shi, *ACS Appl. Mater. Interfaces* **2022**, *14*, 5459.

[15] X. Z. Fan, X. Du, Q. Q. Pang, S. Zhang, Z. Y. Liu, X. Z. Yue, *ACS Appl. Mater. Interfaces* **2022**, *14*, 8549.

[16] Z. Luo, Q. Peng, Z. Huang, L. Wang, Y. Yang, J. Dong, T. T. Isimjan, X. Yang, *J. Colloid Interface Sci.* **2022**, *629*, 111.

[17] J. Qin, H. Liu, P. Zou, R. Zhang, C. Wang, H. L. Xin, *J. Am. Chem. Soc.* **2022**, *144*, 2197.

[18] L. Zong, K. Fan, P. Li, F. Lu, B. Li, L. Wang, *Adv. Energy Mater.* **2022**, *13*, 2203611.

[19] S. Y. Yi, E. Choi, H. Y. Jang, S. Lee, J. Park, D. Choi, Y. Jang, H. Kang, S. Back, S. Jang, J. Lee, *Adv. Mater.* **2023**, *35*, 2302666.

[20] H. Li, J.-J. Zheng, M. Yang, J. Duan, *Nano Res.* **2022**, *16*, 2383.

[21] M. Zhang, H. Li, J. Chen, F. X. Ma, L. Zhen, Z. Wen, C. Y. Xu, *Small* **2022**, *18*, 2202476.

[22] X. Liu, H. Mao, G. Liu, Q. Yu, S. Wu, B. Li, G. Zhou, Z. Li, L. Wang, *Chem. Eng. J.* **2023**, *451*, 138699.

[23] Z. Chen, H. Qing, R. Wang, R. Wu, *Energy Environ. Sci.* **2021**, *14*, 3160.

[24] Y. Cheng, J. Gong, B. Cao, X. Xu, P. Jing, S.-P. Feng, R. Cheng, B. Liu, R. Gao, J. Zhang, *J. Energy Chem.* **2022**, *68*, 646.

[25] D. He, L. Cao, J. Huang, S. Li, Y. Feng, G. Li, F. Wang, L. Feng, *Chem. Eng. J.* **2022**, *429*, 131945.

[26] M. Zhang, H. Li, J. Chen, F. X. Ma, L. Zhen, Z. Wen, C. Y. Xu, *Adv. Funct. Mater.* **2023**, *33*, 2303189.

[27] X. Liu, J. Wu, Z. Luo, P. Liu, Y. Tian, X. Wang, H. Li, *ACS Appl. Mater. Interfaces* **2023**, *15*, 9240.

[28] G. Zhong, S. Xu, L. Liu, C. Z. Zheng, J. Dou, F. Wang, X. Fu, W. Liao, H. Wang, *ChemElectroChem* **2020**, *7*, 1107.

[29] Y. Garsany, O. A. Baturina, K. E. Swider-Lyons, S. S. Kocha, *Anal. Chem.* **2010**, *82*, 6321.

[30] a) Y. Yu, H. Wang, H. Zhang, Y. Tan, Y. Wang, K. Song, B. Yang, L. Yuan, X. Shen, X. Hu, *Electrochim. Acta* **2020**, *334*, 135559; b) C. Lee, K. Shin, C. Jung, P.-P. Choi, G. Henkelman, H. M. Lee, *ACS Catal.* **2019**, *10*, 562.

[31] Q. Liu, X. Wang, L. Li, K. Song, P. Qian, Y. P. Feng, *Nano Res.* **2022**, *15*, 7016.

[32] H. Li, Y. Liu, L. Huang, J. Xin, T. Zhang, P. Liu, L. Chen, W. Guo, T. Gu, G. Wang, *J. Mater. Chem. A* **2023**, *11*, 5179.

[33] K. Li, R. Cheng, Q. Xue, P. Meng, T. Zhao, M. Jiang, M. Guo, H. Li, C. Fu, *Chem. Eng. J.* **2022**, *450*, 137991.

[34] Y. Liu, Z. Chen, Z. Li, N. Zhao, Y. Xie, Y. Du, J. Xuan, D. Xiong, J. Zhou, L. Cai, Y. Yang, *Nano Energy* **2022**, *99*, 107325.

[35] H. Liu, L. Jiang, Y. Sun, J. Khan, B. Feng, J. Xiao, H. Zhang, H. Xie, L. Li, S. Wang, L. Han, *Adv. Energy Mater.* **2023**, *13*, 2301223.

[36] Z. Li, Z. Tian, H. Cheng, T. Wang, W. Zhang, Y. Lu, Y. Lai, G. He, *Energy Storage Mater.* **2023**, *59*, 102764.

[37] C. Zhou, X. Chen, S. Liu, Y. Han, H. Meng, Q. Jiang, S. Zhao, F. Wei, J. Sun, T. Tan, R. Zhang, *J. Am. Chem. Soc.* **2022**, *144*, 2694.

[38] X. Hu, S. Chen, L. Chen, Y. Tian, S. Yao, Z. Lu, X. Zhang, Z. Zhou, *J. Am. Chem. Soc.* **2022**, *144*, 18144.

[39] a) Z. Y. Mei, G. Zhao, C. Xia, S. Cai, Q. Jing, X. Sheng, H. Wang, X. Zou, L. Wang, H. Guo, B. Y. Xia, *Angew. Chem. Int. Ed.* **2023**, *62*, 202303871; b) Y. Ran, C. Xu, D. Ji, H. Zhao, L. Li, Y. Lei, *Nano Research Energy* **2024**, *3*, e9120092.

[40] a) T. Chen, Y. Xu, D. Meng, X. Guo, Y. Zhu, L. Peng, J. Hu, W. Ding, *J. Energy Chem.* **2022**, *71*, 304; b) Q. Wang, Z. L. Zhao, Z. Zhang, T. Feng, R. Zhong, H. Xu, S. T. Pantelides, M. Gu, *Adv. Sci.* **2019**, *7*, 1901279.

RESEARCH ARTICLE
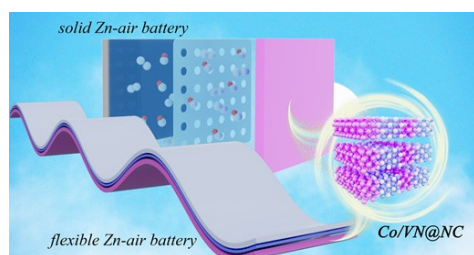
Z. Luo, J. Gong, Q. Li, F. Wei, B. Liu,
Dr. T. Taylor Isimjan*, Prof. Dr. X. Yang*

1 – 10

Geometric and Electronic Engineering in Co/VN Nanoparticles to Boost Bifunctional Oxygen Electrocatalysis for Aqueous/Flexible Zn-Air Batteries

The Co/VN@NC nanofoam exhibits a competitive difference (0.65 V) between the half-wave potential of ORR and OER potential at 10 mA cm^{-2}, leading to an elevated peak power density (156/85 mW cm^{-2}) in aqueous/flexible ZABs. It is attributed to the disordered carbon reinforcing the confinement of electrons, and the coupling of components optimizing the absorption of intermediates.